Explaining an anomalous pressure dependence of shear modulus in germanate glasses based on Reverse Monte Carlo modelling

Sørensen, Søren Strandskov; Ge, Xuan; Micoulaut, Matthieu; Shi, Ying; Juelsholt, Mikkel; M. Ø. Jensen, Kirsten; Neuefeind, Jörg; Jensen, Lars Rosgaard; Bockowski, Michal; Smedskjær, Morten Mattrup

Published in:
Journal of Materials Science & Technology

DOI (link to publication from Publisher):
10.1016/j.jmst.2023.12.051

Publication date:
2024

Document Version
Publisher's PDF, also known as Version of record

Journal of Materials Science & Technology 192 (2024) 54–64

Contents lists available at ScienceDirect

Journal of Materials Science & Technology

journal homepage: www.elsevier.com/locate/jmst

Research Article

Explaining an anomalous pressure dependence of shear modulus in germanate glasses based on Reverse Monte Carlo modelling

Søren S. Sørensen[a,*], Xuan Ge[a], Matthieu Micoulaut[b], Ying Shi[c], Mikkel Juelsholt[d], Kirsten M.Ø. Jensen[d], Jörg Neuefeind[e], Lars R. Jensen[f], Michal Bockowski[g], Morten M. Smedskjaer[a,*]

[a] Department of Chemistry and Bioscience, Aalborg University, DK-9220 Aalborg, Denmark
[b] Sorbonne Université, Laboratoire de Physique Théorique de la Matière Condensée, CNRS UMR 7600, 4 Place Jussieu, 75252 Paris Cedex 05, France
[c] Science and Technology Division, Corning Incorporated, Corning, NY 14831, USA
[d] Department of Chemistry, Copenhagen University, Universitetsparken 5, DK-2100 Copenhagen Ø, Denmark
[e] Neutron Scattering Division, Spallation Neutron Source, Oak Ridge National Laboratory, Oak Ridge, TN 37831, USA
[f] Department of Materials and Production, Aalborg University, DK-9220 Aalborg, Denmark
[g] Institute of High Pressure Physics, Polish Academy of Sciences, 00-142 Warsaw, Poland

ARTICLE INFO

Article history:
Received 6 November 2023
Revised 22 December 2023
Accepted 25 December 2023
Available online 5 February 2024

Keywords:
Glass structure
Diffraction
Densification
Reverse Monte Carlo

ABSTRACT

Unlike traditional silicate glasses, germanate glasses often feature non-monotonic variations in material properties (e.g., elastic moduli and glass transition temperature) with varying chemical composition, temperature, and pressure. However, the underlying atomic-scale structural origins remain poorly understood. This is because, in most oxide glasses, the structural changes are quantified through solid-state NMR spectroscopy, but unfortunately the only NMR active germanium isotope (^{73}Ge) has very unfavorable NMR properties. Here, we circumvent this problem by using high-energy X-ray and neutron total scattering coupled with *ab initio* molecular dynamics simulations as input for Reverse Monte Carlo modeling. In detail, we study the structure and properties of two sodium germanate glasses ($10Na_2O$-$90GeO_2$ and $20Na_2O$-$80GeO_2$) subjected to permanent densification through hot compression up to 2 GPa at the glass transition temperature. While density as well as Young's and bulk modulus increase with pressure as expected, shear modulus first increases and then decreases slightly at higher pressures. The refined atomistic structure models suggest that the glasses feature a distribution of 4, 5, and 6 coordinated Ge with a majority of 4 and 5 coordinated species. Only minor changes in the Ge–O coordination occur upon hot compression, but a notable transformation of edge- to corner-sharing Ge-polyhedra is found. This anomalous polyhedral packing causes a lower number of angular constraints upon higher pressure treatment, explaining the non-monotonic trend of shear modulus with pressure. We also find that the rings become smaller and less circular upon compression, contributing to the volumetric compaction. These findings may aid the future design of germanate glasses with tailored properties and the general understanding of structure-property relations in oxide glasses.

1. Introduction

Germania (GeO_2) is one of the single oxide glass formers and thus analogous to the archetypical silica (SiO_2) glass system [1]. However, in comparison to silicate glasses, germanate glasses are significantly less studied and several questions regarding their thermal, mechanical, and structural properties remain unanswered. This includes the so-called "germanate anomaly", which is the non-monotonic change of properties (e.g., density [2]. glass transition temperature [3], elastic moduli [4], fracture toughness [5], thermal conductivity [5], and non-reversing heat flow [6]) when adding different network modifiers (alkali, alkaline earth, and transition metal oxides) to GeO_2. The underlying structural origin of this effect remains heavily debated, including whether it is due to a change in Ge coordination from 4 to 5 and/or 6 [7–9], or whether it is due to changes in ring-type structures [7,8,10]. As such, the structure-property relations in the germanate glass family are more complex than those of archetypical silicate glasses and

* Corresponding authors.
E-mail addresses: soe@bio.aau.dk (S.S. Sørensen), mos@bio.aau.dk (M.M. Smedskjaer).

https://doi.org/10.1016/j.jmst.2023.12.051

thus more akin to borate glasses [1,11]. This poses challenges for the glass community, but it is also an opportunity to gain a deeper understanding of general structure-property correlations of the oxide glasses. The difficulty in deciphering the structural origins can be largely attributed to the lack of a suitable nuclear magnetic resonance (NMR) active germanium isotope in contrast to the highly NMR suitable isotopes of other network glass formers, such as ^{29}Si, ^{11}B, ^{31}P, and ^{27}Al [12]. Other structural characterization methods are therefore needed. To this end, X-ray and neutron total scattering techniques are ideal due to their ability to extract fundamental information on average coordination in especially simple systems, as well as provide complementary information on structure beyond the short-range order, i.e., medium-range order (MRO).

Apart from composition-induced changes in the germanate glass structure, their non-equilibrium nature also causes the structure to vary as a function of the thermal and pressure history [13]. For example, through compression at low or high temperatures (typically either $<<T_g$ or $\sim T_g$, respectively) [14], commonly coined as cold and hot compression and typically involving either die-type pressing (< 10 GPa), submerging into a liquid pressure transmission medium (> 10 GPa), or using gas pressure chambers (a few GPa) [14]. Both cold and hot compression tends to increase the local coordination number (CN) of liable species in oxide glasses (e.g., B and Al) [15–17], and increasing the temperature during compression generally makes the change in CN greater [16]. The CN contributes to the network densification in, e.g., borate and alumina-containing glasses [15–17]. In other systems, e.g. silicates, no CN number changes are apparent at low pressures (< 10 GPa [14,18]), yet the structure is densified by changes in the MRO [19], such as by reducing ring sizes [20]. Despite a great interest in the pressure response of a variety of glass systems and its impact on structure and properties [13,14,21–26], the pressure response of germanate glasses has not been studied in detail. A notable exception is recent in situ work on pure GeO_2 glass compression under extreme pressures (> 100 GPa), reporting coordination changes with a CN for germanium of up to (or even above) 6 and a CN for oxygen of ~4 [27–30]. These results confirm earlier experimental studies and emphasize an increase in the Ge-O bond distance from 1.73 Å to 1.86 Å upon moderate compression [31], consistent with results from classical molecular dynamics simulations [32,33].

In this work, we focus on a lower pressure regime and employ hot compression (up to 2 GPa of N_2 pressure at T_g) to alter the structure of two sodium germanate glasses ($10Na_2O$-$90GeO_2$ and $20Na_2O$-$80GeO_2$). We then perform structural and mechanical analyses on these permanently densified samples after subsequent cooling and decompression to ambient conditions. In detail, we correlate their mechanical properties with the atomic structure as characterized by state-of-the-art synchrotron and neutron total scattering measurements. Using *ab initio* molecular dynamics (AIMD) simulations, we produce the initial structures of these glasses, which are then refined by Reverse Monte Carlo modelling based on the experimental X-ray and neutron data. We observe a maximum of the shear modulus in both studied glass compositions upon hot compression, which we ascribe to medium-range rather than short-range order structural changes. Namely, significant changes in the inter-polyhedral packing and the packing of Ge–O ring-type structures but only minor distortions of the local Ge–O coordination environment.

2. Materials and methods

2.1. Sample preparation

Base glasses of molar compositions $10Na_2O$-$90GeO_2$ and $20Na_2O$-$80GeO_2$ were prepared by the melt quench method. Specifically, GeO_2 (Chempur, 99.999 %) and Na_2CO_3 (Sigma-Aldrich, > 99.5 %) powders were used as starting materials. The powders were weighed, thoroughly mixed, and added to a $Pt_{90}Rh_{10}$ crucible before heating to ~1300 °C. The melts were then homogenized for 2 h before finally being quenched onto a brass plate. The obtained glasses were annealed at their glass transition temperatures for ~0.5 h (T_g~504 °C and 533 °C for $10Na_2O$-$90GeO_2$ and $20Na_2O$-$80GeO_2$, respectively) before turning off the furnace and letting it cool to RT passively. These glass transition temperatures were probed by differential scanning calorimetry (DSC) by heating from room temperature to ~20 °C above the estimated T_g and then cooling to 200 °C and reheating to ~100 °C above T_g. All heating and cooling scans were done at a rate of 10 K min^{-1}. The T_g was taken as the onset of the glass transition region of the second DSC upscan. We find good agreement with previously measured T_g data [3].

Hot compression of the annealed glasses was performed according to the description in Ref. [16]. In summary, the glasses were compressed in the chamber at 0.5, 1.0, or 2.0 GPa of N_2 gas pressure while being heated to their respective ambient pressure value of T_g. The maximum pressure and temperature were maintained for 30 min before cooling (60 K min^{-1}) under pressure. When reaching room temperature, the pressure was released at a rate of 30 MPa min^{-1}. All following analyses were performed on the permanently densified samples recovered from the hot compression treatment. Permanent here refers to the finding that the glasses remain in their densified state unless they are heated to temperatures around T_g under ambient pressure.

2.2. Mechanical properties

Densities were determined by Archimedes' principle of buoyancy. That is, polished glasses were cut into regular crack-free pieces with a total mass of ~1 g. The mass of the glasses was measured in air (m_{air}) and when submerged in anhydrous ethanol (m_{sub}). Based on the density of ethanol (ρ_{EtOH} = 0.7871 g cm^{-3}), this yields the glass density as,

$$\rho = \frac{\rho_{EtOH} m_{air}}{m_{air} - m_{sub}}. \quad (1)$$

The elastic moduli were determined by measuring the sound velocities using ultrasonic echography with an Olympus 38DL Plus device. Polished glass sheets (~1 mm in thickness) were applied to a longitudinal or transversal ultrasonic wave packet, and the bouncing of the wavepacket on the back of the sample provided an echo that was recorded. This echo is directly related to the longitudinal and transversal speeds of sound (v_L and v_T, respectively) based on knowledge of the sample thickness. The measured density and sound speeds were then used to calculate Young's (E), shear (G), and bulk (B) moduli as well as the Poisson's ratio (υ) [34],

$$E = 2G(1 + \upsilon), \quad (2)$$

$$G = v_T^2 \rho, \quad (3)$$

$$B = \frac{E}{3(1 - 2\upsilon)}, \quad (4)$$

$$\upsilon = \frac{v_L^2 - 2v_T^2}{2\left(v_L^2 - v_T^2\right)}. \quad (5)$$

Vicker's hardness (HV) was determined by micro-indentation using a Struers Duramin 40 indenter equipped with a diamond tip of the Vicker's geometry. The measurements were performed at ambient conditions. Five imprints in each glass were made using a force (P) of 100 gf (0.98 N) and a holding period of 10 s. HV was

then evaluated by measuring the diagonal lengths of the obtained imprints (d) as,

$$HV = 1.854\frac{P}{d^2}. \quad (6)$$

2.3. Structural characterization

Micro-Raman spectra were recorded with a diode laser of 532 nm wavelength equipped on a Renishaw Invia spectroscope. Spectra were normalized by the maximum intensity.

X-ray total scattering experiments were performed at the P02.1 beamline at the Deutsches Elektronen Synchrotron (DESY) in Hamburg, Germany with $\lambda = 0.207$ Å. Prior to beamtime, samples were crushed in a mortar, packed in polyimide (Kapton) capillaries, and sealed using plasticine. The scattering from an empty Kapton capillary was used for background subtraction. Scattering patterns were acquired up to Q~20 Å^{-1} using a measurement time of 5 min. The pattern of an empty Kapton capillary was measured and used as background subtraction. Subsequent data treatments were performed in PDFGetX2 [35] using a procedure described in Ref. [36] to obtain the structure factor, $S(Q)$, and radial distribution function, $G(r)$.

Time-of-flight neutron total scattering experiments were performed at the NOMAD diffractometer at the Spallation Neutron Source (SNS) at Oak Ridge National Lab. Samples were loaded about 2 cm high (~200 mg) into quartz capillaries with an inner diameter of 2.8 mm and an outer diameter of 3 mm. Measurements were conducted for an accelerator proton charge—a proxy for the number of neutrons entering the instrument—of 3 C, corresponding to a measuring time of about 34 min at the time of the experiment. Data were processed by autoNOM, a collection of Python and IDL programs specifically developed for NOMAD. A more comprehensive description of data treatment can be found in Refs. [36,37].

2.4. Molecular dynamics simulations

The Vienna *Ab initio* Simulation Package (VASP) was used to perform AIMD simulations of the studied germanate glasses using the PBEsol pseudopotential and a timestep of 2 fs. Specifically, for each composition, a starting configuration was made based on an archetypical sodium silicate glass of equivalent composition by placing atoms randomly in the simulation box and then performing geometrical optimization using a classical potential [38]. While this procedure did not result in any meaningful structures, it removed the most unphysical structural groups obtained from the random placement of atoms. Next, the density was set according to the experimental densities of the glasses hot compressed at 0, 0.5, 1.0, and 2.0 GPa before structural optimization in the NVT ensemble using an energy cutoff of 400 eV and a convergence criterion of 10^{-1} eV. Next, dynamics were initiated at 4000 K for 5 ps. Then the temperature was instantaneously decreased to 3000 K and the energy cutoff and convergence criteria were set to 600 eV and 10^{-5} eV, respectively. Dynamics were then run for 2 ps in the NVT ensemble. Afterwards, cooling was initiated by first cooling to 2000 K at 200 K ps^{-1} before quenching to 300 K at 1000 K ps^{-1}. The structure was finally relaxed for 1 ps before seeing structural minimization. Densities were in all simulation steps mimicking the experimental values (i.e., volume was fixed in the NVT ensemble). Three quenches of each composition-pressure combination were performed to obtain an adequate amount of independent data sets.

2.5. Reverse Monte Carlo modelling

Since the AIMD simulations only feature 240 atoms, the possibilities for reproducing meaningful MRO structures are severely constrained. To overcome this and enhance the obtained structural models, especially at the MRO scale, we performed reverse Monte Carlo (RMC) modelling on larger structures using the RMC_POT software package [39]. Specifically, cells obtained from AIMD were replicated ($3 \times 3 \times 3$, 6480 atoms) and used as starting structures for the subsequent RMC optimization. We optimized the structures based on the experimental total X-ray and neutron scattering data as well as the short-range partial radial distribution functions (RDFs) of the pairs of NaNa, NaGe, NaO, and OO. The latter were obtained from the AIMD simulations and included for fitting in the 0–7 Å range, while the reciprocal space functions were fitted to their highest Q limits (19 and 47 Å^{-1} for X-ray and neutron total scattering data, respectively). This procedure was performed to ensure meaningful local structuring of especially Na-correlations which are otherwise of very low weight in the total X-ray and neutron scattering data. Furthermore, we provided a large penalty in the RMC optimization for the system when the RMC steps introduced 3-fold coordinated Ge, which effectively restricted the coordination number of Ge to be ≥ 4. Optimizations were run for ~23 h on an 8-core CPU system. The obtained structures were subsequently studied by in-house written code as well as the R.I.N.G.S. software package [40]. The latter was used to quantify the ring size distributions using the primitive rings definition [40].

3. Results and discussion

3.1. Mechanical properties

Similarly, to other glass series [41–43], the hot compression treatment of the two sodium germanate glasses ($10Na_2O$-$90GeO_2$ and $20Na_2O$-$80GeO_2$) induces significant volumetric compaction, as observed from the density variation with pressure in Fig. 1. That is, we find a nearly linear increase in density with increasing hot compression pressure. The slope of the density vs. pressure provides the so-called plastic compressibility ($\beta = V^{-1}dV/dP^{-1}$, where V is volume and P is pressure) which is a relative measure of how much the glass compacts per unit pressure. For both studied germanate glasses ($10Na_2O$-$90GeO_2$ and $20Na_2O$-$80GeO_2$), we find $\beta \approx 0.025$ GPa^{-1}, which is in the same range as that of other oxide glass compositions, e.g., in the aluminosilicate family [14,44].

The measured longitudinal and transversal sound velocities (Fig. S1 in Supporting Information) are then combined with the density data to estimate the elastic moduli (Fig. 2). Young's and bulk moduli (Fig. 2(a, b)) feature a common tendency of increasing modulus with increasing hot compression pressure, but with a signif-

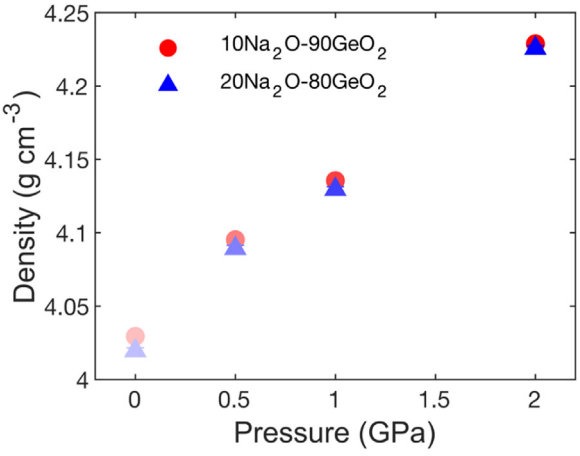

Fig. 1. Densities of $10Na_2O$-$90GeO_2$ (red circles) and $20Na_2O$-$80GeO_2$ (blue triangles) glasses upon hot compression at 0, 0.5, 1.0, and 2.0 GPa. Error bars are smaller than the size of the symbols. The intensity of the color describes the pressure (most pale: 0 GPa; most intense: 2.0 GPa).

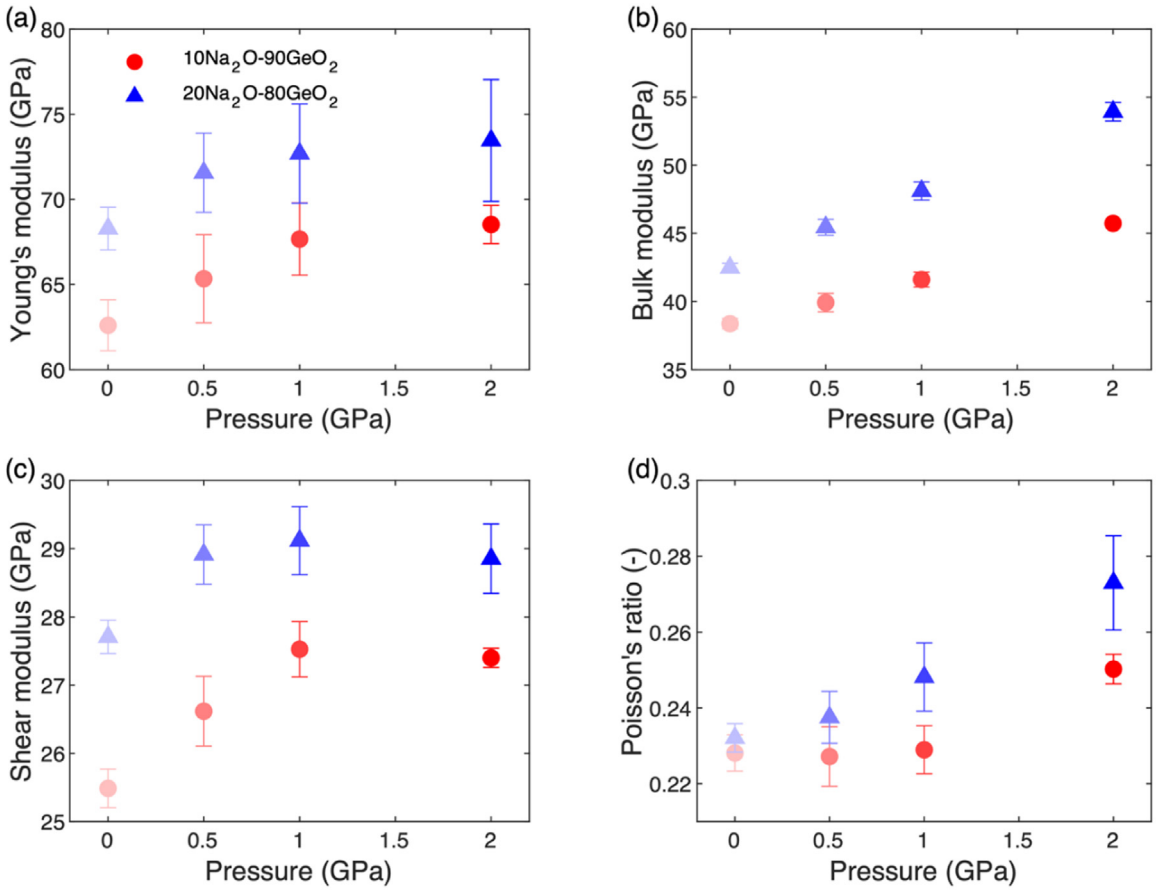

Fig. 2. (a) Young's, (b) shear, and (c) bulk moduli as well as (d) Poisson's ratio of $10Na_2O$-$90GeO_2$ (red circles) and $20Na_2O$-$80GeO_2$ (blue triangles) upon hot compression at 0, 0.5, 1.0, and 2.0 GPa. The intensity of the color describes the pressure (most pale: 0 GPa; most intense: 2.0 GPa).

icantly smaller change in Young's modulus per unit pressure at higher pressures. This trend of increasing modulus with increasing pressure has previously been observed in numerous oxide glass systems [15,44–46] and may be primarily ascribed to the general increase in atomic packing density [47]. We also tested the Vicker's hardness of the glasses (Fig. S2), finding a similar increase with increasing pressure due to the higher number of bond constraints per unit of volume in the densified glasses.

Shear modulus (Fig. 2(c)) shows an interesting non-monotonic trend, with an initial increase in modulus in the 0–1 GPa pressure range, but then a slight decrease in modulus in the 1–2 GPa pressure range. This "anomalous" behavior stands in stark contrast to the common observation of monotonically increasing elastic moduli with increasing density [47]. Interestingly, pure SiO_2 glass also features pressure anomalies with known decreases of both bulk and shear moduli upon in situ cold compression [20,48,49]. This decrease in the case of SiO_2 is, however, initiated upon pressure changes already at ambient pressure and has its extrema (minimum) around 2 GPa. The structural origin is commonly associated with conformational changes of small rings (containing around six Si atoms), related to the ring structures found in crystalline α- and β-cristabolite [20]. The fact that we only observe the non-monotonic trend in the case of shear modulus in the studied germanate glasses is thus especially interesting. Lastly, Poisson's ratio (Fig. 2(d)) shows another unusual non-linear behavior, with a significant increase with pressure, most pronounced at the highest pressures. Notably, the $20Na_2O$-$80GeO_2$ glass exhibits an increase in Poisson's ratio of ~20 % upon treatment at 2 GPa compared to the initial state, which is a larger increase compared to that of most other oxide glasses [14,44,50].

3.2. Experimental structure characterization

To understand the structural origins of these changes in mechanics upon hot compression of the $10Na_2O$-$90GeO_2$ and $20Na_2O$-$80GeO_2$ glasses, we have used a variety of structural characterization. Starting with Raman spectroscopy (results presented in Fig. S3), we find only minor changes in the spectra with increasing pressure, likely associated with slight changes in the asymmetric stretching vibrations within the Ge-polyhedra [51] and mainly for the $20Na_2O$-$80GeO_2$ glasses in the band at ~870 cm^{-1}.

We therefore focus on the X-ray and neutron total scattering (Q_{max} of ~20 $Å^{-1}$ and ~45 $Å^{-1}$ for X-ray and neutron, respectively) data collected at the Petra III synchrotron and Spallation Neutron Source at Oak Ridge National Lab, respectively. We note that the X-ray and neutron experiments provide complementary information, yet with some differences due to the X-ray and neutron scattering lengths. For the present samples this means that atomic correlations from Ge provide significantly higher intensities in the X-ray as compared to the neutron data (see also the discussion below). The measured scattering data provide the reciprocal space structure factor, $F(Q) = (S(Q)–1)Q$, and can be used to deduce further information about the glass structure. The low-Q region of $F(Q)$ is presented in Fig. 3, where stronger color represents increasing hot compression pressure in each plot. The full Q-range is presented in Fig. S4. We find no major change across the full Q-range with pressure for neither X-ray nor neutron scattering data. However, considering the low-Q region (Fig. 3(a)), minor changes are notable for both glass compositions. It is generally agreed that the low-Q features are related to the MRO glass structure [52,53] and that pressurization generally causes shifts to higher Q values. This

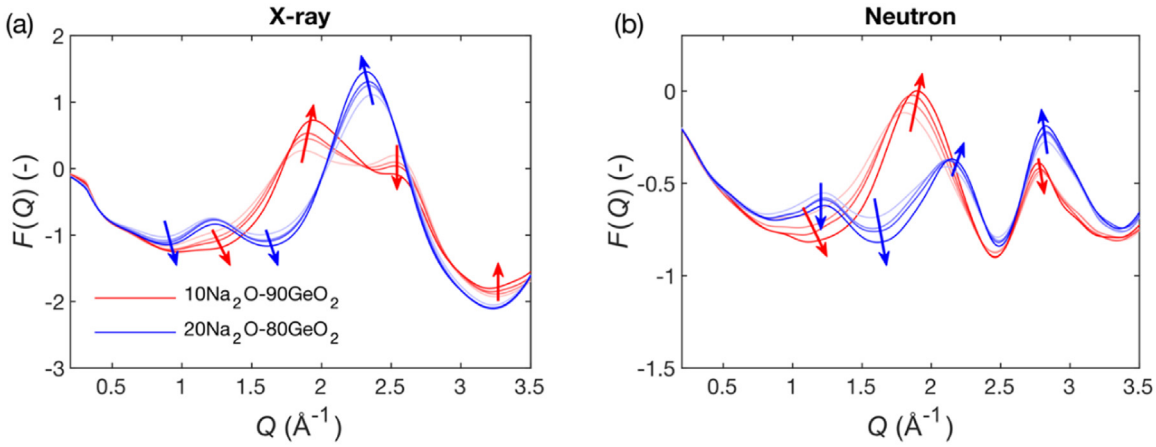

Fig. 3. (a) X-ray and (b) neutron structure factor $F(Q)$ of $10Na_2O$-$90GeO_2$ (red curves) and $20Na_2O$-$80GeO_2$ (blue curves) upon hot compression at 0, 0.5, 1.0, and 2.0 GPa of N_2 gas pressure. The intensity of the color describes the pressure (most pale: 0 GPa; most intense: 2.0 GPa).

is because the position of the first sharp diffraction peak (FSDP), i.e., the peak at the lowest Q-value, is argued to be proportional to $Q_1 = 2\pi d^{-1}$, where d is interplanar spacing [52–54]. A notable exception is the $20Na_2O$-$80GeO_2$ data in Fig. 3(a). Taken as a whole, these findings suggest that the observed densification (Fig. 1) is mainly governed by MRO structural changes, yet some MRO structural features move further apart upon pressurization. This MRO dependence is partly in contrast to observation for other network-forming species with more than one available coordination state, e.g., B and Al. Although not accounting for the complete volumetric densification, these species show a pronounced increase in their coordination number (i.e., short-range order structure as obtained from both scattering and NMR) upon hot compression at 1–2 GPa [17,45,55] in addition to changes in medium-range structural ordering [56].

The X-ray data suffers from how X-ray atomic scattering factors have a strong Q-dependence, often making it difficult to extract coordination numbers from X-ray data, including from the present data. However, the neutron data has constant scattering factors [57] and thus offers the opportunity to easier extract Ge coordination numbers. This is done through the radial distribution function ($g(r)$, see Fig. S5 for a variant of the RDF given by $G(r) = [g(r)–1]4\pi r\rho_0$) [58,59]. Assuming that all contributions of the first peak (maximum at ~1.9 Å) are due to the Ge–O correlation, the cumulative oxygen coordination number of Ge can be estimated as,

$$\mathrm{CN}(r) = 4\pi\rho_0 c_O \int_0^r \left(r'\right)^2 g_{GeO}(r)\mathrm{d}r', \tag{7}$$

where,

$$g_{GeO}(r) = \frac{g(r)\left(\sum_i c_i b_i\right)^2}{2b_O b_{Ge} c_O c_{Ge}}. \tag{8}$$

Here, ρ_0 is the atomic number density, c_i is the fraction of the ith atom in the system, b_i is the neutron scattering length of the ith atom in the system, r is the atomic separation, g_{GeO} is the radial distribution function, and $g(r)$ is the total radial distribution function. We note that this equation is only valid if $g(r)$ only features contributions from the Ge–O correlation, but this is a good assumption up until at least the minimum between the first two peaks (~2.2 Å). The calculated cumulative oxygen coordination around Ge is shown in Fig. 4. The $10Na_2O$-$90GeO_2$ glasses exhibit practically constant Ge–O coordination, while the $20Na_2O$-$80GeO_2$ glasses show a slight increase in Ge–O coordination with pressure. This is similar to the case of silicate glasses [61], but in contrast

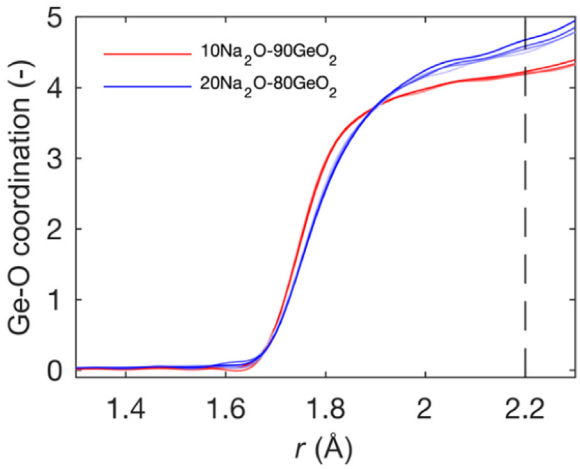

Fig. 4. Cumulative Ge coordination number for all $10Na_2O$-$90GeO_2$ (red curves) and $20Na_2O$-$80GeO_2$ (blue curves) glasses prepared under four different hot compression pressures (0, 0.5, 1.0, and 2.0 GPa). The intensity of the color describes the pressure (most pale: 0 GPa; most intense: 2.0 GPa).

to observations from B and Al-containing glasses at similar pressures, with pronounced coordination changes observed at pressures of few GPa [16,42,62–65]. Similarly, the observed pressure-induced coordination change is much lower than a previous estimation based on Raman spectroscopy of a molten $Na_2Ge_2O_5{\cdot}H_2O$ system compressed to ~2.2 GPa, reporting a conversion of more than half of 4-fold coordinated Ge species to 6-fold coordinated Ge [66] —possibly due to either misinterpretation of the collected Raman signal, a higher liability of CN change in the liquid, or due to the presence of water in the structure. The estimated Ge coordination numbers of the present glasses are summarized in Table 1, where those of the pristine glasses are compared to previous estimations from the literature. Overall, this analysis suggests that local coordination number changes should only play a minor role in

Table 1
Average Ge coordination numbers as calculated from the neutron scattering data at a separation of 2.2 Å. Previous estimates of the average coordination for the two ambient glasses (from Ref. [60]) are presented in brackets.

	0 GPa	0.5 GPa	1.0 GPa	2.0 GPa
$10Na_2O$-$90GeO_2$	4.21 (4.25)	4.21	4.19	4.23
$20Na_2O$-$80GeO_2$	4.49 (4.44)	4.55	4.59	4.68

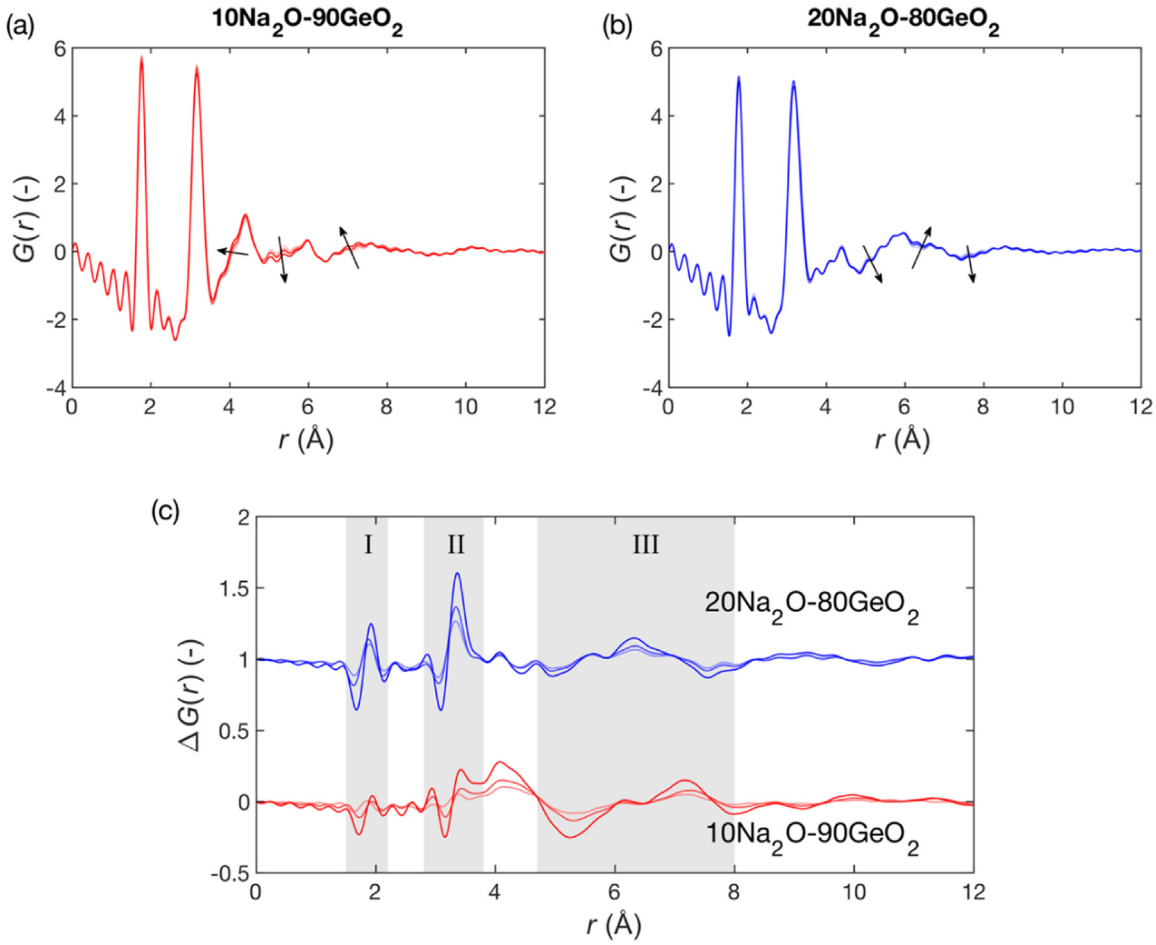

Fig. 5. Examples of X-ray radial distribution functions of (a) $10Na_2O$-$90GeO_2$ and (b) $20Na_2O$-$80GeO_2$ glasses prepared under four different hot compression pressures (0, 0.5, 1.0, and 2.0 GPa). (c) Difference plot ($\Delta G(r)$) of the radial distribution functions of the two studied sodium germanate glasses as subtracted by the RDF at 0 GPa with data of the $20Na_2O$-$80GeO_2$ glasses shifted by +1. The intensity of the color describes the pressure (most pale: 0 GPa; most intense: 2.0 GPa). Arrows in panels (a, b) indicate changes with increasing pressure treatment.

controlling the observed changes in compaction and elastic moduli (Fig. 2).

While the neutron scattering data offers reliable estimations of the average Ge CN, it provides a somewhat biased view of the atomic correlations depending on the neutron scattering lengths (b_{Na} = 3.63 fm, b_{Ge} = 8.185 fm, b_O = 5.803 fm). To achieve complementary information on the structural changes upon hot compression, we therefore also consider the collected X-ray total scattering data, because these scattering lengths are proportional to the number of electrons of the element. That is, the intensity of the pair-correlations including heavy elements is more intense in the X-ray RDFs. For the present sodium germanate glasses, this is relevant because Ge (Z = 32) is significantly heavier than O (Z = 8) and Na (Z = 11), i.e., correlations including Ge are significantly more intense in the X-ray RDFs as seen by the intense peak at ~3.3 Å (due to the Ge–Ge correlation) in Fig. 5. Also notably, these data show systematic changes with increasing pressure denoted by arrows in Fig. 5. Such changes are not found to the same extent in the neutron RDFs (see Fig. S5), which only feature minor changes upon hot compression. This suggests that it is mainly the Ge-correlations beyond the short-range order structure that are affected by densification, i.e., the underlying base GeO_2 network is more sensitive to pressure than the Na-related subnetwork.

We also plot the difference between the ambient case and pressure-treated cases in Fig. 5(c) using a difference function (i.e., the RDF of densified glass is subtracted by that of the 0 GPa glass). We find that the main changes occur in three distinct regions, namely: (I) Ge–O correlation, which shifts to higher r-values, indicating minor or no increasing coordination (in agreement with the neutron data, see Fig. 4); (II) Ge–Ge correlation, which also shifts to higher r and becomes more dominant, indicating changes in the inter-polyhedral packing with Ge-polyhedra correlations moving further apart; and (III) medium-range order structures, likely associated with, e.g., ring-type structure packing. We furthermore show various zooms of Fig. 5(a, b) in Fig. S6.

3.3. RMC optimized atomic configurations

To gain more insights into the details of the structural compaction mechanism in sodium germanate glasses, we follow a computational approach. First, we have prepared both $10Na_2O$-$90GeO_2$ and $20Na_2O$-$80GeO_2$ glasses at four different levels of densification (similar to the experiments) using AIMD simulations in VASP. Three repetitions for each combination of composition and pressure were prepared, giving a total of 24 independent simulations. We mimic the densification experiments by fixing the volume of each case to the measured experimental density of the glasses (as presented in Fig. 1). Comparing the obtained structures with the experimental scattering data (Fig. S7), we find overall good agreement between simulations and experiments, especially for the high Q-range (short-range order structure), yet with some differences at very low Q-range features (medium-range order). To address this

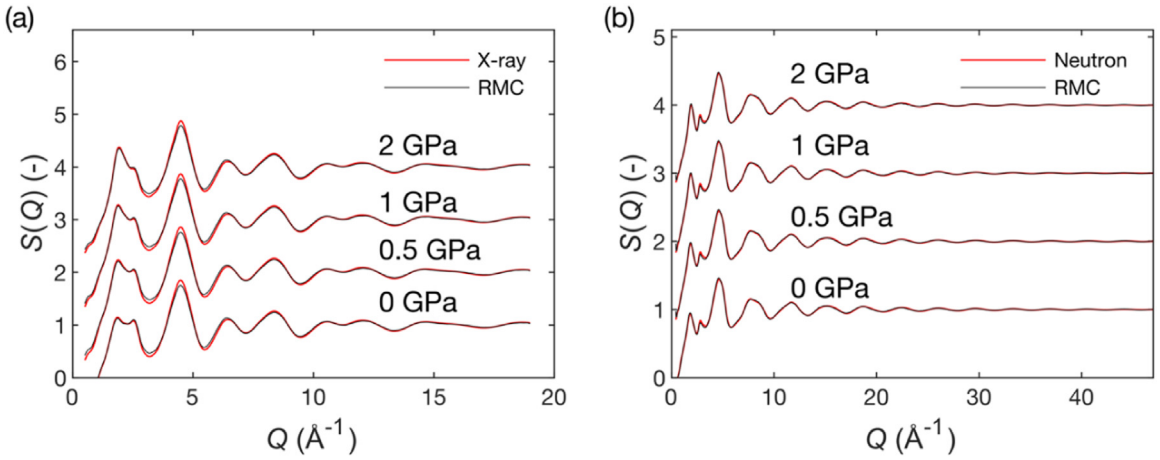

Fig. 6. Comparison of measured (a) X-ray and (b) neutron structure factors ($S(Q)$) calculated from RMC structures (black curve) and experiments (red curve) for all studied $10Na_2O$-$90GeO_2$ glasses.

issue, we use the AIMD data together with the experimental densities and X-ray and neutron total scattering data as input for RMC optimization. In detail, we replicate the final structure from the AIMD simulations into 3 × 3 × 3 supercells, followed by RMC optimization using a cost-function composed of weights from (1) estimated Ge–O coordination numbers (Table 1); (2) the fitting to partial short-range RDFs for all pair correlations from AIMD simulations; and (3) experimental X-ray and neutron total structure factors. Furthermore, we have included a significant penalty to the cost function if/when the RMC optimization introduces three-fold coordinated Ge to solely allow for Ge–O coordination states of ≥ 4 in the final structures.

Using these RMC-optimized structures for the 24 different glass samples (two compositions, four densities, three repetitions), we find very good agreement with the experimental X-ray and neutron structure factors (Figs. 6 and S8). For example, data for the ambient pressure $10Na_2O$-$90GeO_2$ glass is found in Fig. 6(a, b) for X-ray and neutron scattering, respectively. This suggests that these atomistic models provide excellent structural descriptions of the alkali germanate structures, offering an opportunity for probing the distribution of coordination numbers of Ge in the studied glasses – something which is otherwise very challenging for Ge. By extracting the coordination environments of Ge–O from the RMC structures, we find that it closely matches that of the experimental average Ge coordination (as expected given that the RMC structures were fitted against this parameter). In detail, we find a distribution of coordination states (Ge–O coordination of 4–6, as illustrated and discussed in more detail below), yet with a clear prevalence for the 4- and 5-fold coordinated states (~55 %–80 % and ~20 %–40 % of the total Ge, respectively), leaving the 6-fold coordinated state as a minority (~1 %–5 %). These findings parallel those found for the compressed base network GeO_2 glass, where 5-fold Ge is obviously present [67] and 6-fold are minority sites up to 22 GPa [68]. The highest fractions of 5- and 6-fold coordinated species are found in the $20Na_2O$-$80GeO_2$ glasses, as expected considering their higher average coordination number (Fig. 4). Given the known cases of both 5- and 6-coordinated Ge in crystalline germanate species [69,70], the suggested distribution among all three coordination states seems meaningful, also when considering how, e.g., also the CN of Si in alkali silicates can be 4–6 at high pressures [71]. We also probed the coordination states of oxygens (Tables S1 and S2) to find somewhat constant fractions (mostly less than 1 % change upon pressure treatment) of non-bridging, bridging, and even some tricluster oxygens upon the different pressure treatments. The presence of the three coordination states of Ge (4–6), as well as the different oxygen species (non-bridging, bridging, and tricluster), agree well with the results in a previous simulation study on $2Na_2O$-$9GeO_2$ glass [72].

In addition to the scattering functions and coordination states, the obtained RMC structures allow for more detailed atomistic characterization such as the bond-angle distribution of both the intra-polyhedral O–Ge–O angles (Fig. 7(a)) as well as the inter-polyhedral Ge–O–Ge angles (Fig. 7(b)). Fig. 7(a) shows that the O–Ge–O angles vary from ~60° and up to ~180°, yet with a clear abundance of angles in the range of 80°–120°. This demonstrates the variation of the polyhedral coordination with an abundance of the ideal tetrahedron configuration (~109°), but also with distinct five- and six-fold coordinated environments (which involve specific angles of 90°, 120°, and 180°). Interestingly, a feature around 60° is also identified, which is attributed to species of edge-sharing polyhedra, which have also previously been identified in a simulation study of a $2Na_2O$-$9GeO_2$ glass [72]. Now, increasing the pressure causes the O–Ge–O angles to move to slighter lower values, which is likely associated with a slight increase in coordination number. For the angles at ~60°, there seems to be a slight decrease in intensity with increasing pressure, suggesting a decrease in the edge-sharing species with increasing pressure, possibly associated with the slight increase in the overall Ge coordination. We note that such edge-sharing motifs are absent in pure GeO_2 glass, which is a completely tetrahedral network, but they appear once the Ge coordination increases upon Na addition. The presence of the edge-sharing motifs is independently confirmed by the observation that the typical Ge–Ge correlating distance in the corresponding partial pair correlation function matches well with that of other edge-sharing species in Ge chalcogenides [73].

These observations are supported by the results from the Ge–O–Ge angles (Fig. 7(b)), where a broad distribution is found in the range of 100°–180°, somewhat in contrast to the narrower distribution observed in pure GeO_2 glass [74]. This difference may be because pure GeO_2 only features tetrahedral Ge while the present sodium germanates feature a range of different coordination species. The latter originates mainly from the bridging oxygen species connecting Ge polyhedra through corner-sharing polyhedra. However, again there seems to be a lower-angle shoulder peak (at ~80°–100°), which we ascribe to the edge-sharing species. Like the case of the O–Ge–O angles, the intensity of this shoulder peak slightly decreases with increasing pressure, again pointing towards fewer edge-sharing species with increasing pressure.

The available RMC-optimized structures allow for complete deduction of the degree of edge-sharing. Notably, we quantify the

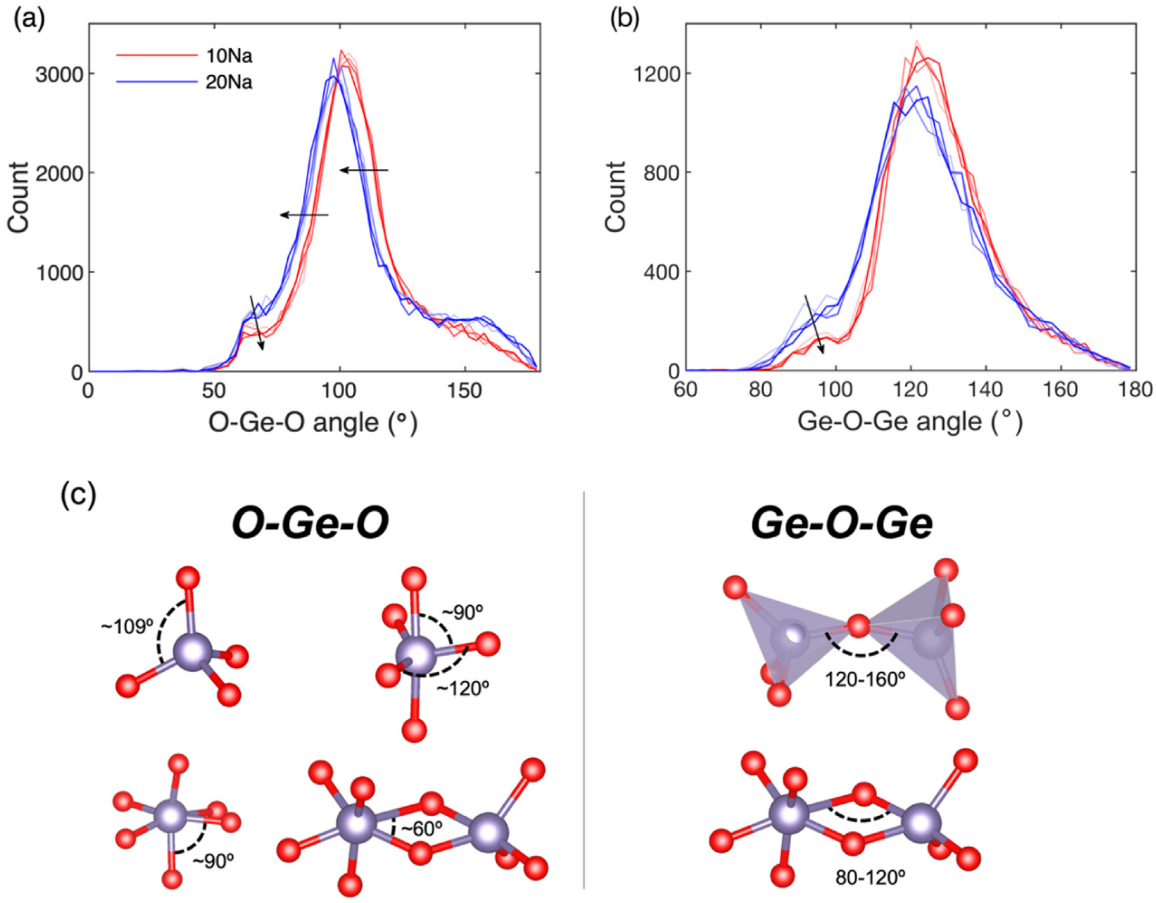

Fig. 7. Bond angle distributions of (a) O–Ge–O and (b) Ge–O–Ge obtained from the RMC optimized structures of $10Na_2O$-$90GeO_2$ (red curves) and $20Na_2O$-$80GeO_2$ (blue curves) glasses upon hot compression at 0, 0.5, 1.0, and 2.0 GPa. The intensity of the color describes the pressure (most pale: 0 GPa; most intense: 2.0 GPa). (c) Overview of structural origins of different bond angles of the O–Ge–O and Ge–O–Ge bond angle distributions.

amount of edge- and corner-sharing polyhedra in Tables S3 and S4, finding a decrease of edge-sharing upon increasing pressure with total changes on a scale of 2 %–3 % with a larger effect for the $20Na_2O$-$80GeO_2$ glass (drop from ~13 % to ~11 % of edge-sharing species). Further experimental support for the edge-sharing interpretation is found in the X-ray RDFs (Fig. 5 and zooms found in Fig. S6), showing an increase in the correlation length for the peak around 3.15 Å (stemming from the Ge–Ge correlations) with pressure, as caused by the partial separation of the edge-sharing species into corner-sharing. We note that crystalline sodium enneagermanate ($Na_4Ge_9O_{20}$) is well-known for featuring stable edge-sharing Ge-polyhedra while being obtainable by crystallization from glassy sodium germanate [70]. Other crystalline alkali germanates are also known to feature edge-sharing [75]. Finally, the pressurized GeO_2 network former also displays an increasing population of edge-sharing motifs upon compression as more and more 5-fold Ge emerge [68].

The edge-sharing of polyhedra represents the simplest case of an ABAB ring-type structure (here –Ge–O–Ge–O–). To quantify this as well as the fractions of larger ring-type structures, we compute the ring size distributions (see Methods). The results of this analysis are shown in Fig. 8. We find that the extent of edge-sharing (i.e., the ring size with two Ge atoms in Fig. 8 as well as Tables S3 and S4) indeed decreases with increasing pressure for both glass compositions, thus in agreement with the bond-angle distribution analysis in Fig. 7. However, the ring analysis also provides information on much larger rings (with up to 11 Ge atoms). Notably, the $10Na_2O$-$90GeO_2$ glass features larger rings compared to the $20Na_2O$-$80GeO_2$ glass. Specifically, while the $10Na_2O$-$90GeO_2$ glass mainly features rings with a size of 5–6 Ge atoms, the $20Na_2O$-$80GeO_2$ glass has smaller rings (with 3–4 Ge atoms). Both the studied compositions, however, feature rings in the same size range (2–10 Ge atoms). Considering next the pressure dependence of the ring size distribution, we find again that increasing pressure leads to a shift towards smaller rings, especially in the range of ring sizes of 6–10 Ge atoms. In contrast, the fraction of smaller rings (3–5 Ge atoms) does not change significantly with the pressure treatment. While the ring size distribution is a fundamental tool to understand what governs the structural changes beyond the short-range order, it only counts the length of rings, but provides no information about the ring shape. We note that the latter has recently been found to be important for glass properties [76].

To evaluate the ring topology, we start by fitting a plane to the atom positions of each ring and then evaluate the planarity of the ring by computing the average distance of each atom to the fitted plane. This analysis shows a general trend of increasing distances from the plane with the ring size (from ~0.1 Å to ~0.8 for ring sizes from 2 to 10 Ge, respectively), yet with no significant pressure dependence (Fig. S9(a)). Next, we fit an ellipse to each ring structure identified by RINGS to obtain information on the best fit of the semi-minor (b) and semi-major axis (a) distances, i.e., the distances from the center of the ellipse to the closest and most distance point on the ellipse (see schematic drawing in Fig. 9). From these two distances, we calculate the average ring radius ($(a + b)/2$), which increases with increasing ring size (Fig. S9(b)). Finally, from the minor- and major axis distances, we also

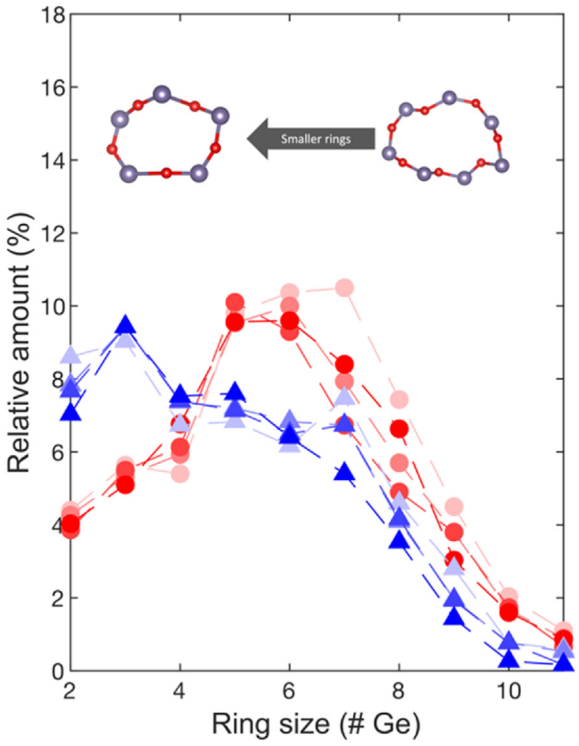

Fig. 8. Ring size distribution of the $10Na_2O$-$90GeO_2$ (red curves) and $20Na_2O$-$80GeO_2$ (blue curves) glasses upon hot compression at 0, 0.5, 1.0, and 2.0 GPa. The intensity of the color describes the pressure (most pale: 0 GPa; most intense: 2.0 GPa). An example of the involved ring-type structures is shown as an inset.

calculate the so-called ring eccentricity (ε),

$$\varepsilon = \sqrt{1 - \frac{b^2}{a^2}}. \quad (9)$$

The eccentricity of a perfect circle will be 0, while an ellipse will exhibit $0 < \varepsilon < 1$, with higher ε values corresponding to more distorted ellipses.

The calculated ring eccentricity for the studied $10Na_2O$-$90GeO_2$ and $20Na_2O$-$80GeO_2$ glasses at the four different pressures is shown in Fig. 9(a). For the smallest rings, we find relatively large eccentricity, likely because the edge-sharing rings feature significant differences in the size of the included atoms, creating rather distorted ellipses. However, for larger rings ($\geq$ 3 Ge atoms), we generally find an increasing eccentricity with increasing ring size for both glass compositions (see the example of increasing eccentricity in Fig. 9(b)). This is because perfect circular fits are less likely with the increasing complexity introduced by the increasing number of atoms. In contrast to the above analysis from plane and ellipse fitting (Fig. S9), the eccentricity systematically increases with increasing pressure (Fig. 9(a)). This suggests that rings with $\geq$ 4 Ge atoms become more distorted (elongated) with increasing pressure for both glass compositions.

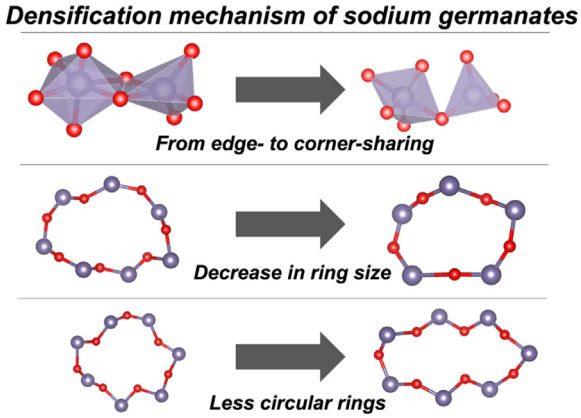

Fig. 10. Schematic illustration of the proposed structural densification mechanisms of the studied sodium germanate glasses upon hot compression treatment.

3.4. Structural densification mechanism

Since we have found that the Ge CN is relatively unaffected by the hot compression treatment (Table 1), we ascribe the volumetric densification of both sodium germanate glasses to a combination of (1) polyhedra featuring less edge- and more corner-sharing with increasing pressure; and (2) decrease in ring sizes with increased pressure; and (3) elongation of rings towards being more elliptical upon hot compression. We summarized these structural effects in Fig. 10.

Such structural compaction mechanisms including decreasing ring sizes and distortion of ring shapes are comparable to observations in other oxide glasses, e.g., pure SiO_2 glass which exhibits

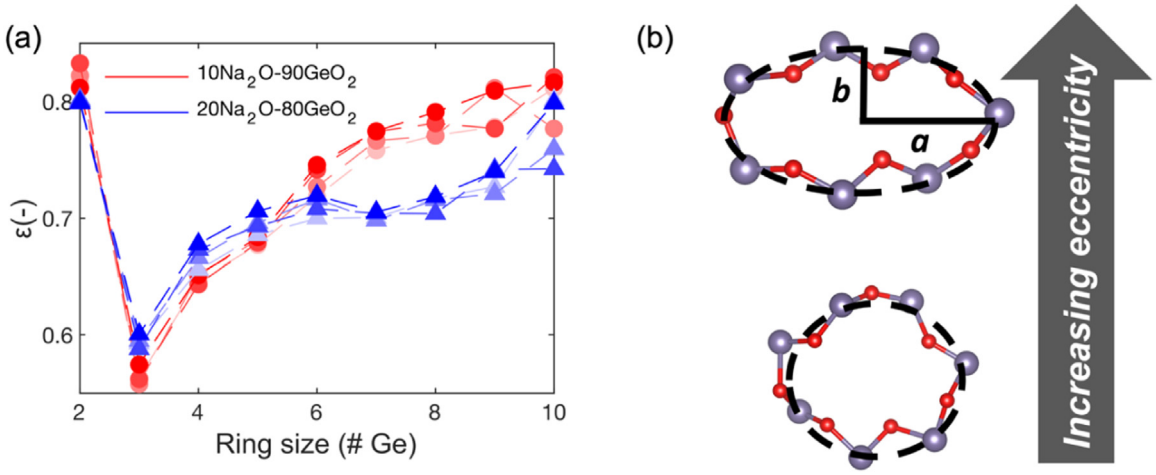

Fig. 9. (a) Eccentricity (ε, if circular: $\varepsilon = 0$; if elliptical: $0 < \varepsilon < 1$) for RMC optimized structures of (red) $10Na_2O$-$90GeO_2$ and (blue) $20Na_2O$-$80GeO_2$ after hot compression at 0, 0.5, 1.0, and 2.0 GPa of N_2 gas pressure. Stronger color indicates higher pressure in the range of 0 to 2 GPa. (b) A sketch of increasing eccentricity.

significant ring-type changes with pressure increase [20]. This includes, e.g., zipping of rings [77], where larger rings upon compaction "divide" into two sub-rings, likely explaining our ring size decrease and the presence of some tricluster oxygens (Tables S1 and S2). However, the observed mechanism of partial transformation from edge- to corner-sharing differs from that of many other oxide glasses. For example, pure SiO_2 glass is generally tetrahedral and corner-sharing at ambient conditions but undergoes a transition from corner- to edge-sharing upon a significant pressure increase ($>$ 10 GPa) significantly below the glass transition [78]. Similarly, pure GeO_2 glass tends to feature edge-sharing only after high-pressure/high-temperature treatment [79,80]. However, we note that crystalline sodium enneagermanate has a significant fraction of edge-sharing between Ge-polyhedra [70], likely explaining why such species are indeed identified in our sodium germanate glass structures. Interestingly, we find the mechanism of edge- to corner-sharing to be more pronounced for the $20Na_2O$-$80GeO_2$ glass compared to the $10Na_2O$-$90GeO_2$ glass (see Figs. 7 and 8), albeit present in both systems. In turn, the $10Na_2O$-$90GeO_2$ glass seems to be slightly more affected by ring distortion compared to the $20Na_2O$-$80GeO_2$ glass (Fig. 9). However, the overall compaction mechanisms appear to be similar between the two studied sodium germanate glass compositions.

3.5. Structure-property relations

Finally, we attempt to connect the above structural information with the elastic properties (Fig. 2), especially the non-monotonic trend in shear modulus with pressure. Notably, unlike glassy SiO_2 which features anomalous (decreasing) shear and bulk modulus for even small increases in pressure, the present sodium germanates first see an anomaly above $\sim$1 GPa, and only for the shear modulus (Fig. 2(c)), while the change in bulk modulus is monotonic (Fig. 2(b)). This suggests that the inherent anomaly mechanisms between pure SiO_2 and the presently studied sodium germanate glasses are somewhat different. We note that up until 1 GPa of hot compression, both Young's, bulk, and shear moduli increase, likely mainly driven by the overall compaction of the structure through ring size decrease and elongation. This is the case for both of the studied sodium germanate compositions. Now, while it is well-established that the anomaly in the case of glassy SiO_2 is caused by a ring-conformation change (from β- to α-cristobalite conformations) [20], we here suggest that the studied sodium germanates feature a slight decrease in shear modulus at $>$ 1 GPa due to the transformation of edge- to corner- sharing Ge polyhedra. The transition from edge- to corner-sharing allows for the rotation around the Ge–O–Ge bond axis in more polyhedra and a significant reduction in the resistance to shear deformation. This can be understood from a rigidity point-of-view [81,82], since the bond angles, especially for the bridging oxygens, in the edge-sharing polyhedra are more constrained than those in the corner-sharing case. Upon transforming the edge-sharing polyhedra into the corner-sharing ones at elevated pressure, the inter-polyhedral angles feature fewer atomic constraints and thus allow for easier shear deformation, even though the overall structure densifies significantly. While mostly apparent for the shear modulus, this effect also slightly affects Young's modulus (Fig. 2(a)). As such, while we do also find the transformation of edge- to corner-sharing at lower pressure treatments (0–1 GPa, see Table S3), the mixture of different compaction mechanisms (ring size and ring conformity changes) and following increasing density likely hides this effect on the shear modulus in the 0–1 GPa pressure range. To our knowledge, the edge- to corner-sharing transformation upon *increasing* pressure has not previously been observed in other oxide glasses and may thus provide a new way of tailoring glass properties and understanding their structure-property relations.

4. Conclusions

We have studied the response of two sodium germanate glasses ($10Na_2O$-$90GeO_2$ and $20Na_2O$-$80GeO_2$) to hot compression up to 2 GPa. We find that the structures densify with pressure and the elastic moduli also generally increase upon hot compression, although notably the shear modulus slightly decreases for hot compression above 1 GPa. We investigate the structural origins through Reverse Monte Carlo optimization of the structures with input from X-ray and neutron total scattering data as well as AIMD simulations, finding that the sodium germanates feature a combination of 4-, 5-, and 6-fold coordinated Ge species as well as a significant fraction of edge-sharing polyhedra. Interestingly, we find that upon hot compression, the fraction of edge-sharing decreases as these units are partially substituted for corner-sharing polyhedra. We ascribe this structural transformation to be responsible for the anomalous (non-monotonic) pressure dependence of shear modulus since the number of bond-angle constraints decreases with the transformation from edge- to corner-sharing, despite the overall increase in density of the structure. Our work thus provides novel structural insight to the sodium germanate glass family and sheds new light on structure-property relations of oxide glasses in general.

Declaration of competing interest

The authors declare that they have no known competing financial interests or personal relationships that could have appeared to influence the work reported in this paper.

Acknowledgments

This work was supported by grants from the European Union (ERC, NewGLASS, No. 101044664) and the MSCA Postdoctoral Fellowship (No. 101062110) from the Horizon Europe Framework Programme. Views and opinions expressed are, however, those of the authors only and do not necessarily reflect those of the European Union or the European Research Council. Neither the European Union nor the granting authority can be held responsible for them. We acknowledge the computational resources supplied by EuroHPC Joint Undertaking with access to Vega at IZUM, Slovenia (No. EHPC-REG-2022R02–224) and Aalborg University (No. CLAAUDIA). Mikkel Juelsholt and Kirsten M. Ø. Jensen are grateful for funding from the Villum Foundation (No. VKR00015416). We also acknowledge DESY (Hamburg, Germany), a member of the Helmholtz Association HGF, for the provision of experimental facilities. The X-ray total scattering experiments were carried out at beamline P02.1 at PETRA III, and we would like to thank Martin Etter for his assistance in using the beamline. We furthermore thank DANSCATT (supported by the Danish Agency for Science and Higher Education) for support. A portion of this research also used resources at the Spallation Neutron Source, a DOE Office of Science User Facility operated by the Oak Ridge National Laboratory.

Supplementary materials

Supplementary material associated with this article can be found, in the online version, at doi:10.1016/j.jmst.2023.12.051.

References

[1] A.K. Varshneya, Fundamentals of Inorganic Glasses, Elsevier, Netherlands, 2013.
[2] M.K. Murthy, J. Ip, Nature 201 (1964) 285–286.
[3] M.M. Ashton-Patton, Ph.D. Thesis, Alfred University, 2013.
[4] A. Osaka, K. Takahashi, K. Ariyoshi, J. Non.-Cryst. Solids 70 (1985) 243–252.

[5] S.S. Sørensen, T. To, J.F.S. Christensen, H. Johra, M.M. Smedskjaer, J. Am. Ceram. Soc. 105 (2022) 977–989.
[6] K. Rompicharla, D.I. Novita, P. Chen, P. Boolchand, M. Micoulaut, W. Huff, J. Phys.- Condens. Matter 20 (2008) 202101.
[7] H.M. Wang, G.S. Henderson, Phys. Chem. Glasses 46 (2005) 377–380.
[8] G.S. Henderson, H.M. Wang, Eur. J. Mineral. 14 (2002) 733–744.
[9] O.L.G. Alderman, A.C. Hannon, S. Feller, R. Beanland, D. Holland, J. Phys. Chem. C 121 (2017) 9462–9479.
[10] G.S. Henderson, M.E. Fleet, J. Non-Cryst. Solids 134 (1991) 259–269.
[11] J.E. Shelby, Introduction to Glass Science and Technology, 2nd ed., The Royal Society of Chemistry, UK, 2005.
[12] R. Youngman, Materials (Basel) 11 (2018) 476.
[13] M.M. Smedskjaer, R.E. Youngman, S. Striepe, M. Potuzak, U. Bauer, J. Deubener, H. Behrens, J.C. Mauro, Y. Yue, Sci. Rep. 4 (2014) 3770.
[14] T. Du, S.S. Sørensen, T. To, M.M. Smedskjaer, J. Appl. Phys. 131 (2022) 170901.
[15] M. Guerette, M.R. Ackerson, J. Thomas, F. Yuan, E.B. Watson, D. Walker, L. Huang, Sci. Rep. 5 (2015) 15343.
[16] S. Kapoor, L. Wondraczek, M.M. Smedskjaer, Front. Mater. 4 (2017) 1.
[17] S. Kapoor, X. Guo, R.E. Youngman, C.L. Hogue, J.C. Mauro, S.J. Rzoska, M. Bockowski, L.R. Jensen, M.M. Smedskjaer, Phys. Rev. Appl. 7 (2017) 1–16.
[18] Y. Kono, Y. Shu, C. Kenney-Benson, Y. Wang, G. Shen, Phys. Rev. Lett. 125 (2020) 205701.
[19] E.J. Kim, Y.H. Kim, S.K. Lee, J. Phys. Chem. C 123 (2019) 26608–26622.
[20] L. Huang, F. Yuan, M. Guerette, Q. Zhao, S. Sundararaman, J. Mater. Res. 32 (2017) 174–182.
[21] Y. Kono, Y. Shibazaki, C. Kenney-Benson, Y. Wang, G. Shen, Proc. Natl. Acad. Sci. U. S. A. 115 (2018) 1742–1747.
[22] P.S. Salmon, A. Zeidler, J. Phys.-Condens. Matter 27 (2015) 133201.
[23] H.T.T. Ta, A.K. Tieu, H. Zhu, H. Yu, N.V. Tran, T.D. Ta, J. Phys. Chem. B 124 (2020) 277–287.
[24] M.N. Svenson, M. Guerette, L. Huang, M.M. Smedskjaer, J. Non-Cryst. Solids 443 (2016) 130–135.
[25] C. Prescher, V.B. Prakapenka, J. Stefanski, S. Jahn, L.B. Skinner, Y. Wang, Proc. Natl. Acad. Sci. U. S. A. 114 (2017) 10041–10046.
[26] A. Yamada, S.J. Gaudio, C.E. Lesher, J. Phys. Conf. Ser. 215 (2010) 012085.
[27] Y.H. Kim, Y.S. Yi, H.I. Kim, P. Chow, Y. Xiao, G. Shen, S.K. Lee, J. Am. Chem. Soc. 144 (2022) 10025–10033.
[28] Y. Kono, C. Kenney-Benson, D. Ikuta, Y. Shibazaki, Y. Wang, G. Shen, A. Navrotsky, Proc. Natl. Acad. Sci. U. S. A. 113 (2016) 3436–3441.
[29] K. Matsutani, A. Yamauchi, S. Kasamatsu, T. Usuki, J. Phys. Soc. Jpn. 91 (2022) 124601.
[30] X. Hong, M. Newville, Y. Ding, J. Phys.-Condens. Matter 35 (2023) 164001.
[31] J.P. Itie, A. Polian, G. Calas, J. Petiau, A. Fontaine, H. Tolentino, Phys. Rev. Lett. 63 (1989) 398.
[32] M. Micoulaut, J. Phys.-Condens. Matter 16 (2004) L131.
[33] M. Micoulaut, Y. Guissani, B. Guillot, Phys. Rev. E 73 (2006) 031504.
[34] G. Mavko, T. Mukerji, J. Dvorkin, The Rock Physics Handbook, Cambridge University Press, Cambridge, UK, 2020.
[35] X. Qiu, J.W. Thompson, S.J.L. Billinge, J. Appl. Crystallogr. 37 (2004) 678.
[36] Y. Shi, N.T. Lonnroth, R.E. Youngman, S.J. Rzoska, M. Bockowski, M.M. Smedskjaer, J. Non.-Cryst. Solids 483 (2018) 50–59.
[37] Y. Shi, B. Deng, O. Gulbiten, M. Bauchy, Q. Zhou, J. Neuefeind, S.R. Elliott, N.J. Smith, D.C. Allan, Nat. Commun. 14 (2023) 13.
[38] S.H. Hahn, J. Rimsza, L. Criscenti, W. Sun, L. Deng, J. Du, T. Liang, S.B. Sinnott, A.C.T. Van Duin, J. Phys. Chem. C 122 (2018) 19613–19624.
[39] O. Gereben, L. Pusztai, J. Comput. Chem. 33 (2012) 2285–2291.
[40] S.Le Roux, P. Jund, Comput. Mater. Sci. 49 (2010) 70–83.
[41] M.M. Smedskjaer, S.J. Rzoska, M. Bockowski, J.C. Mauro, J. Chem. Phys. 140 (2014) 054511.
[42] T. To, S.S. Sørensen, J.F.S. Christensen, R. Christensen, L.R. Jensen, M. Bockowski, M. Bauchy, M.M. Smedskjaer, ACS Appl. Mater. Interfaces 13 (2021) 17753–17765.
[43] L. Ding, K.H. Lee, T. Zhao, Y. Yang, M. Bockowski, B. Ziebarth, Q. Wang, J. Ren, M.M. Smedskjaer, J.C. Mauro, J. Am. Ceram. Soc. 103 (2020) 6215–6225.
[44] M.N. Svenson, M. Guerette, L. Huang, N. Lönnroth, J.C. Mauro, S.J. Rzoska, M. Bockowski, M.M. Smedskjaer, Chem. Phys. Lett. 651 (2016) 88–91.
[45] S.S. Sørensen, M.S. Bødker, H. Johra, R.E. Youngman, S.L. Logunov, M. Bockowski, S.J. Rzoska, J.C. Mauro, M.M. Smedskjaer, J. Non-Cryst. Solids 557 (2021) 120644.
[46] P. Liu, A.L.S. Søndergaard, R.E. Youngman, S.J. Rzoska, M. Bockowski, L.R. Jensen, M.M. Smedskjaer, J. Am. Ceram. Soc. 104 (2021) 1345–1359.
[47] C. Kittel, Introduction to Solid State Physics, 8th ed., Wiley, New York, USA, 2005.
[48] K. Kondo, S. Iio, A. Sawaoka, J. Appl. Phys. 52 (1981) 2826–2831.
[49] W. Schill, S. Heyden, S. Conti, M. Ortiz, J. Mech. Phys. Solids 113 (2018) 105–125.
[50] T. Deschamps, J. Margueritat, C. Martinet, A. Mermet, B. Champagnon, Sci. Rep. 4 (2014) 7193.
[51] H. Verweij, J.H.J.M. Buster, J. Non-Cryst. Solids 34 (1979) 81–99.
[52] Q. Zhou, Y. Shi, B. Deng, J. Neuefeind, M. Bauchy, Sci. Adv. 7 (2021) eabh1761.
[53] Q. Mei, C.J. Benmore, S. Sen, R. Sharma, J.L. Yarger, Phys. Rev. B 78 (2008) 144204.
[54] Y. Shi, J. Neuefeind, D. Ma, K. Page, L.A. Lamberson, N.J. Smith, A. Tandia, A.P. Song, J. Non-Cryst. Solids 516 (2019) 71–81.
[55] S. Li, J.J. Kweon, S. Lee, A.C. Lee, S.K. Lee, J. Phys. Chem. Lett. 14 (2023) 2078–2086.
[56] S.K. Lee, A.C. Lee, J.J. Kweon, J. Phys. Chem. Lett. 12 (2021) 1330–1338.
[57] V.F. Sears, Neutron News 3 (1992) 26–37.
[58] D.A. Keen, J. Appl. Crystallogr. 34 (2001) 172–177.
[59] P.F. Peterson, D. Olds, M.T. McDonnell, K. Page, J. Appl. Crystallogr. 54 (2021) 317–332.
[60] M. Ueno, M. Misawa, K. Suzuki, Physica B+C 120 (1983) 347–351.
[61] J.F. Stebbins, Encyclopedia of Glass Science, Technology, History, and Culture I, Wiley, New York, USA, 2021.
[62] S. Kapoor, R.E. Youngman, L. Ma, N. Lönnroth, S.J. Rzoska, M. Bockowski, L.R. Jensen, M. Bauchy, M.M. Smedskjaer, Front. Mater. 6 (2019) 1–13.
[63] J. Wu, J. Deubener, J.F. Stebbins, L. Grygarova, H. Behrens, L. Wondraczek, Y. Yue, J. Chem. Phys. 131 (2009) 104504.
[64] K. Rompicharla, D.I. Novita, P. Chen, P. Boolchand, M. Micoulaut, W. Huff, J. Phys.- Condens. Matter 337 (2004) 196–200.
[65] L. Wondraczek, S. Sen, H. Behrens, R.E. Youngman, Phys. Rev. B 76 (2007) 014202.
[66] D.L. Farber, Q. Williams, Science 256 (1992) 1427–1430.
[67] G. Lelong, L. Cormier, G. Ferlat, V. Giordano, G.S. Henderson, A. Shukla, G. Calas, Phys. Rev. B 85 (2012) 2–7.
[68] M. Micoulaut, X. Yuan, L.W. Hobbs, J. Non-Cryst. Solids 353 (2007) 1961–1965.
[69] H. V, A.W.E. Fay, in: Zeitschrift Für Kristallographie, 138, Kristallgeometrie, Kristallphysik, Kristallchemie, 1973, pp. 439–448.
[70] M.E. Fleet, S. Muthupari, J. Solid State Chem. 140 (1998) 175–181.
[71] J.F. Stebbins, S. Bista, J. Non-Cryst. Solids 505 (2019) 234–240.
[72] T. Nanba, J. Kieffer, Y. Miura, J. Non-Cryst. Solids 277 (2000) 188–206.
[73] S. Chakraborty, P. Boolchand, M. Micoulaut, Phys. Rev. B 96 (2017) 094205.
[74] J. Neuefeind, K.D. Liss, Berichte Der Bunsengesellschaft Für Physikalische Chemie 100 (1996) 1341–1349.
[75] D. Cabaret, F. Mauri, G.S. Henderson, Phys. Rev. B 75 (2007) 184205.
[76] E.J. Pedersen, T. To, S.S. Sørensen, R. Christensen, J.F.S. Christensen, L.R. Jensen, M. Bockowski, O.V. Magdysyuk, M. Diaz-Lopez, Y. Yue, M.M. Smedskjaer, Phys. Rev. Mater. 7 (2023) 053607.
[77] A. Zeidler, K. Wezka, R.F. Rowlands, D.A.J. Whittaker, P.S. Salmon, A. Polidori, J.W.E. Drewitt, S. Klotz, H.E. Fischer, M.C. Wilding, C.L. Bull, M.G. Tucker, M. Wilson, Phys. Rev. Lett. 113 (2014) 135501.
[78] A. Hasmy, S. Ispas, B. Hehlen, Nature 599 (2021) 62–66.
[79] J. Haines, J.M. Leâ, C. Chateau, A.S. Pereira, Phys. Chem. Miner. 27 (2000) 575–582.
[80] G.S. Smith, P.B. Isaacs, Acta Cryst. 17 (1964) 842.
[81] J.C. Mauro, Am. Ceram. Soc. Bull. 90 (2011) 31–37.
[82] M.F. Thorpe, J. Non.-Cryst. Solids 57 (1983) 355–370.